

SCIENTIFIC REPORTS



Correction: Author Correction

OPEN

Double MgO-based Perpendicular Magnetic-Tunnel-Junction Spin-valve Structure with a Top $\text{Co}_2\text{Fe}_6\text{B}_2$ Free Layer using a Single SyAF $[\text{Co}/\text{Pt}]_n$ Layer

Jin-Young Choi¹, Dong-gi Lee¹, Jong-Ung Baek² & Jea-Gun Park^{1,2}

A new perpendicular spin-transfer-torque magnetic-tunnel-junction (p-MTJ) spin-valve was developed to achieve a high tunneling magnetoresistance (TMR) ratio. It had a double MgO-based spin-valve structure with a top $\text{Co}_2\text{Fe}_6\text{B}_2$ free layer and incorporated a single SyAF $[\text{Co}(0.4\text{ nm})/\text{Pt}(0.3\text{ nm})]_3$ layer and a new buffer layer of $\text{Co}(0.6)/\text{Pt}(0.3)/\text{Co}(0.4)$. It had a TMR ratio of 180% and anisotropy exchange field (H_{ex}) of 3.44 kOe after *ex-situ* annealing of 350 °C for 30 min under a vacuum below 10^{-6} torr and a perpendicular magnetic field of 3 tesla, thereby ensuring a memory margin and avoiding read disturbance failures. Its high level of performance was due to the face-center-cubic crystallinity of the MgO tunneling barrier being significantly improved by decreasing its surface roughness (i.e., peak-to-valley length of 1.4 nm).

Perpendicular spin-transfer-torque magnetic random access memory (p-STT MRAM) has been intensively researched because of its possible applications in various new memory devices and neuromorphic devices^{1–4}. p-STT MRAM has many advantages over current memory devices, such as non-volatility, fast read/write speed (~ 10 ns), extremely low power consumption (< 1 pJ/bit), high write endurance ($> 10^{12}$), and scalability^{5,6}. In particular, attempts have been made to use p-STT MRAM as an embedded memory in systems-on-chip for mobile and internet-of-things applications^{7,8}. In addition, terabit integration of p-STT MRAM cells has been investigated as a way to make a stand-alone memory device that would be a solution to the scaling limitations of dynamic random access memory below the 10-nm design rule. Furthermore, the p-STT MRAM concept has recently been expanded to include spin-neuron and synapse devices^{3,4}. p-STT MRAM cells consist of a selective device and a perpendicular magnetic tunneling junction (p-MTJ) spin-valve^{9–11}. A lot of research has gone into improving three device parameters of these spin-valves. The tunneling magnetoresistance (TMR) ratio for ensuring a memory margin should be greater than 150%. The thermal stability ($\Delta = K_u V / k_B T$) necessary for a ten-year retention-time should be above 74, where K_u is the magnetic anisotropy energy, V is the volume of the free layer, k_B is the Boltzmann constant, and T is the temperature. The switching current density J_{CO} of about 1 MA/cm² must be achieved for low power consumption. Moreover, these device parameters should be available at a back end of line (BEOL) temperature of > 350 °C^{12,13}. Note that BEOL process is the fabrication process to integrate the memory cells which include metal line interconnection, metal line isolation, passivation, and etc. The BEOL temperature (> 350 °C) represents the temperature required during the BEOL process. To enhance these device parameters at the BEOL temperature, p-MTJ spin-valve structures have been developed to withstand temperatures greater than 350 °C. For example, the previous bottom CoFeB free layer has been changed to a top CoFeB free layer for increasing the TMR ratio¹⁴ and the single MgO-based p-MTJ spin-valve design has been changed to a double MgO-based p-MTJ spin-valve design for enhancing thermal stability^{15–17}. In addition, it has been shown that a p-MTJ spin-valve incorporating a tungsten (W) based seed, bridging, and capping layer, instead of the tantalum (Ta) used in our previous study, enhances both the TMR ratio and thermal stability^{14,18,19}.

¹MRAM Center, Department of Electronics and Computer Engineering, Hanyang University, Seoul, 133-791, Republic of Korea. ²MRAM Center, Department of Nanoscale Semiconductor Engineering, Hanyang University, Seoul, 04763, Republic of Korea. Correspondence and requests for materials should be addressed to J.-G.P. (email: parkjgl@hanyang.ac.kr)

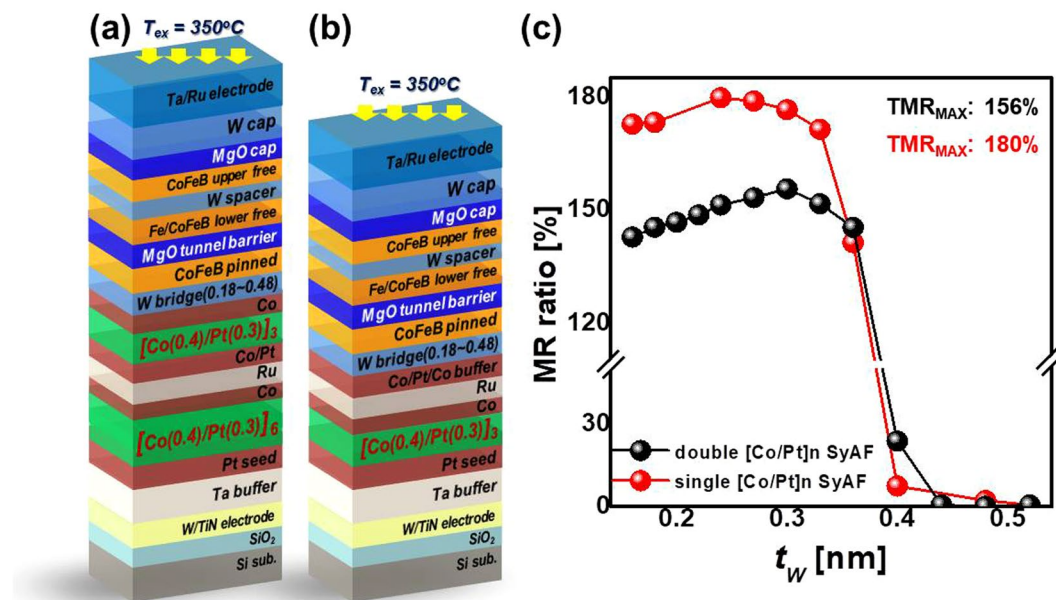


Figure 1. Dependency of the TMR ratio on p-MTJ spin-valve structure. Schemes of double MgO based p-MTJ spin-valve with a top $\text{Co}_2\text{Fe}_6\text{B}_2$ free layer using (a) a double SyAF $[\text{Co}/\text{Pt}]_n$ layers, (b) a single SyAF $[\text{Co}/\text{Pt}]_n$ layer, (c) TMR ratio depending on W bridge-layer thickness (t_w) and p-MTJ spin-valve structure.

However, a double MgO-based p-MTJ spin-valve structure with a top CoFeB free layer remains a challenging target, because the roughness of the MgO tunneling barrier lower the TMR ratio^{20–24}. Thus, in the study reported here, we designed a new double MgO-based p-MTJ spin-valve structure with a top CoFeB free layer using a single synthetic anti-ferromagnetic (SyAF) $[\text{Co}/\text{Pt}]_n$ layer instead of a double SyAF $[\text{Co}/\text{Pt}]_n$ layer that greatly reduces the roughness of the tunneling barrier, as shown in Fig. 1. First, we investigated the dependency of the TMR ratio on the body-centered-cubic (b.c.c) W bridge layer thickness for a double MgO-based p-MTJ spin-valve with a top $\text{Co}_2\text{Fe}_6\text{B}_2$ free layer using a single SyAF $[\text{Co}/\text{Pt}]_n$ layer [Fig. 1(b)] and compared it with that of a double MgO-based p-MTJ spin-valve with a top $\text{Co}_2\text{Fe}_6\text{B}_2$ free layer using a double SyAF $[\text{Co}/\text{Pt}]_n$ layer [i.e., the conventional SyAF $[\text{Co}/\text{Pt}]_n$ layer: Fig. 1(a)]. Second, to understand the magnetic properties that differentiate the TMR ratio, we analyzed the static spin-torque-transfer behavior of the two different p-MTJ spin-valves by using vibrating sampling magnetometer (VSM). Third, to determine the reason for the TMR ratio difference, we observed the face-centered-cubic (f.c.c) crystallinity of the MgO tunneling barrier and $\text{Co}_2\text{Fe}_6\text{B}_2$ pinned layer of both spin-valves by using cross-sectional high-resolution-transmission-electron-microscopy (x-HRTEM). Finally, to investigate the dependencies of the current-vs.-voltage (I-V) curve, parallel-to-antiparallel switching voltage ($V_{P\text{-to-}AP}$), antiparallel-to-parallel switching voltage ($V_{AP\text{-to-}P}$), reading current in the low- or high-resistance state (I_P or I_{AP}), and the normalized TMR ratio-vs.-voltage curve on the structure of SyAF $[\text{Co}/\text{Pt}]_n$ layer (i.e., a single or double), we fabricated p-MTJ spin-valve cells with a 34-nm diameter bottom electrode and 60 μm -diameter top-electrode (see Supplement 1).

Results

TMR ratio of p-MTJ spin-valves. The dependency of the TMR ratio on the W bridge layer thickness (t_w) was investigated as a function of the structure of SyAF $[\text{Co}/\text{Pt}]_n$ layer, as shown in Fig. 1(c). For the double MgO-based p-MTJ spin-valve with a top $\text{Co}_2\text{Fe}_6\text{B}_2$ free layer using the double SyAF $[\text{Co}/\text{Pt}]_n$ layer (i.e., the conventional SyAF $[\text{Co}/\text{Pt}]_n$ layer), there was a slight increase in the TMR ratio for t_w values up to around 0.3 nm, since the ferro-coupling strength slightly increased with t_w . The TMR ratio abruptly decreased when t_w exceeded 0.36 nm, because the ferro-coupling strength between the upper $[\text{Co}/\text{Pt}]_3$ SyAF layer and the $\text{Co}_2\text{Fe}_6\text{B}_2$ pinned layer weakened abruptly. Thus, the maximum TMR ratio was only about 156% at a t_w of 0.3 nm. On the other hand, the TMR ratio of the spin-valve with a top $\text{Co}_2\text{Fe}_6\text{B}_2$ free layer using a single SyAF $[\text{Co}/\text{Pt}]_n$ layer slightly increased up to a t_w of 0.24 nm and then slightly decreased between t_w values of 0.24 nm and 0.36 nm. The TMR ratio then rapidly decreased for t_w values greater than 0.36 nm. Thus, the TMR ratio reached 180% at a t_w of 0.24 nm. The dependency of the TMR ratio on t_w for the p-MTJ spin-valve using the single SyAF $[\text{Co}/\text{Pt}]_n$ layer was similar to that of the spin-valve using the double SyAF $[\text{Co}/\text{Pt}]_n$ layer. However, the TMR ratio of the spin-valve using the single SyAF $[\text{Co}/\text{Pt}]_n$ layer (i.e., 180%) was much higher than that of the one using the double SyAF $[\text{Co}/\text{Pt}]_n$ layer (i.e., 156%). In particular, this means that the Co (0.6 nm)/Pt (0.3 nm)/Co (0.4 nm) bridging buffer layer shown in Fig. 1(b) was well designed for anti-ferro-coupling the single SyAF $[\text{Co}/\text{Pt}]_3$ layer to the $\text{Co}_2\text{Fe}_6\text{B}_2$ pinned layer.

Magnetic properties of p-MTJ spin-valves. To clarify the magnetic properties of the spin-valves with the single SyAF $[\text{Co}/\text{Pt}]_n$ layers, we investigated the static magnetic momentum-vs.-applied magnetic field (M - H) loops as a function of t_w , as shown in Fig. 2. The M - H loops of the spin-valves with a top $\text{Co}_2\text{Fe}_6\text{B}_2$ free layer using the double SyAF $[\text{Co}/\text{Pt}]_n$ layer [Fig. 2(a–c)] were compared with those of the spin-valves with a top $\text{Co}_2\text{Fe}_6\text{B}_2$ free

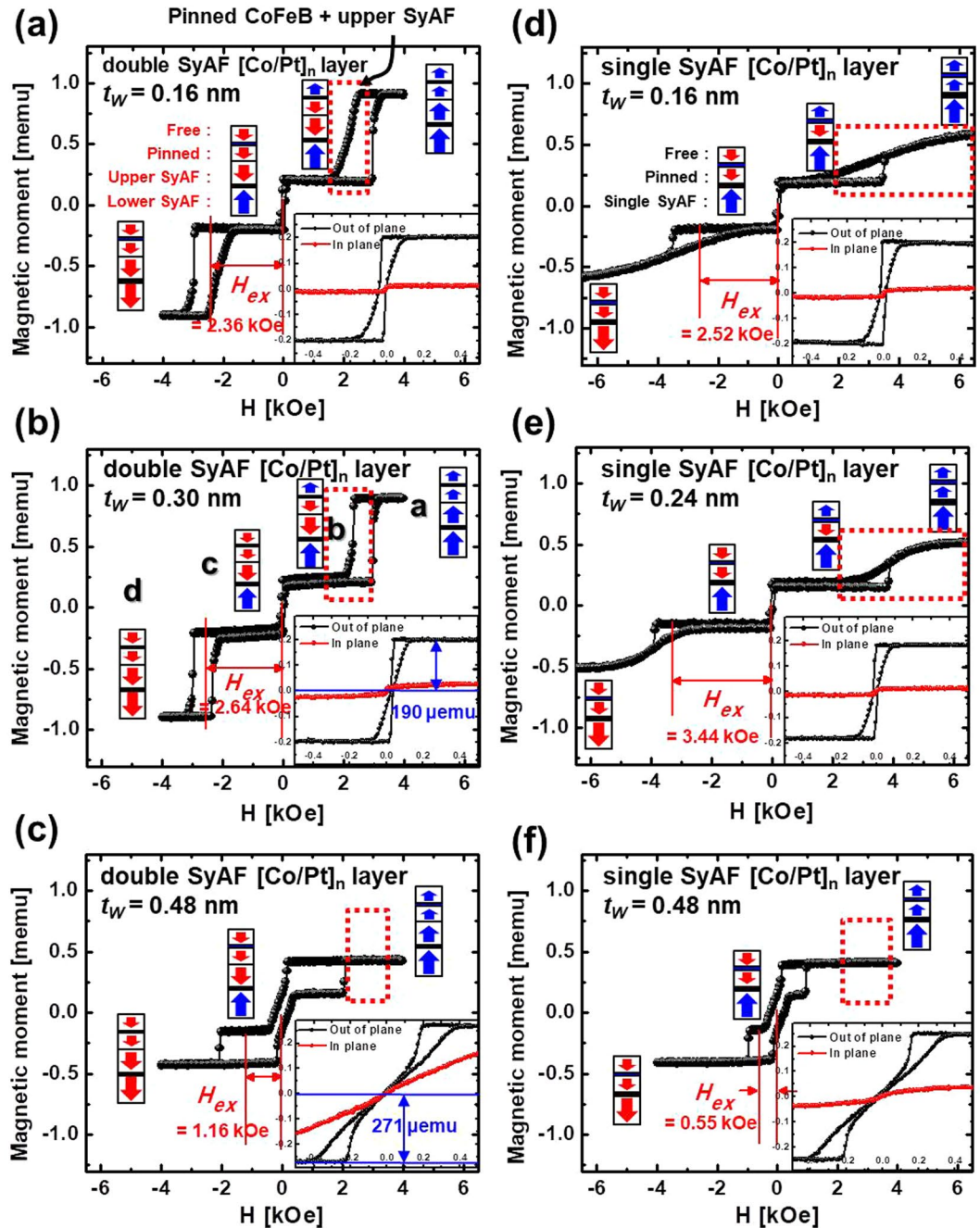


Figure 2. Dependency of static magnetic behavior (magnetic moments-vs.-applied magnetic field) on p-MTJ spin-valve structure and t_w bridge-layer thickness (t_w). P-MTJ spin-valve with a double SyAF $[\text{Co/Pt}]_n$ layer and (a) $t_w = 0.16$ nm, (b) $t_w = 0.30$ nm, (c) $t_w = 0.48$ nm. P-MTJ spin-valve with a single SyAF $[\text{Co/Pt}]_n$ layer and (d) $t_w = 0.16$ nm, (e) $t_w = 0.30$ nm, (f) $t_w = 0.48$ nm.

layer using the single SyAF $[\text{Co/Pt}]_n$ layer [Fig. 2(d-f)]. In the case of the spin-valves using the double SyAF $[\text{Co/Pt}]_n$ layer, at t_w of 0.16 nm, the spin-electron direction of the upper SyAF $[\text{Co/Pt}]_6$ layer ferro-coupled with the $\text{Co}_2\text{Fe}_6\text{B}_2$ pinned layer rotated from upward to downward when the external perpendicular magnetic-field (H) was scanned from +4 to +1.5 kOe, as shown in Fig. 2(a). Moreover, the spin-electron direction of the $\text{Co}_2\text{Fe}_6\text{B}_2$ free layer rotated from upward to downward when H was scanned from +0.2 to -0.2 kOe, showing that free layer had good perpendicular magnetic characteristics (i.e., the M - H loop showed good squareness) and its magnetic moment was ~ 0.2 memu, as shown in the inset of Fig. 2(a). The spin-electron direction of the lower SyAF $[\text{Co/Pt}]_3$ layer then rotated from upward to downward and the magnetic moment of the spin-valve saturated at 0.91 memu when H was scanned from -1.5 to -4 kOe. As a result, at a t_w of 0.16 nm, the spin-valve had an anisotropy exchange field (H_{ex}) of 2.36 kOe (Fig. 2(a)). Next, when t_w was changed from 0.16 to 0.30 nm, the squareness of the M - H loops of both the upper SyAF $[\text{Co/Pt}]_3$ layer ferro-coupled with the $\text{Co}_2\text{Fe}_6\text{B}_2$ pinned layer and the

lower SyAF [Co/Pt]₆ layer considerably improved (compare the red boxes in Fig. 2(a) and (b)). In addition, the squareness of the *M-H* loop of the Co₂Fe₆B₂ free layer slightly improved, resulting in an increase of the TMR ratio from 143 to 156%, (see the insets of Fig. 2(a), Fig. 2(b), and Fig. 1(c)). Recall that the ferro-coupling strength between the upper SyAF [Co/Pt]₃ layer and the Co₂Fe₆B₂ pinned layer directly affect the TMR ratio; i.e., a higher ferro-coupling strength leads to a higher TMR ratio²⁵. Furthermore, H_{ex} of the spin-valve increased slightly from 2.36 to 2.64 kOe, which would make the spin-valve more susceptible to read disturbance. Otherwise, when t_W was increased from 0.30 to 0.48 nm, the *M-H* loop of the spin-valve changed abnormally because the thicker t_W could not perfectly ferro-couple the upper SyAF [Co/Pt]₃ layer with the Co₂Fe₆B₂ pinned layer (see the red box in Fig. 2(c)). In particular, the squareness of the *M-H* loop of the Co₂Fe₆B₂ free layer drastically deteriorated, resulting in the TMR ratio falling from 156 to 0% (the insets of Fig. 2(b) and (c)). Note that the magnetic moment increased from 190 to 271 μ emu, indicating that the upper SyAF [Co/Pt]₃ layer did not completely ferro-couple with the Co₂Fe₆B₂ pinned layer since the magnetic moment of the Co₂Fe₆B₂ free layer was only 190 μ emu. In addition, H_{ex} of the spin-valve greatly decreased from 2.64 to 1.16 kOe, which would cause a read failure.

In contrast, for the p-MTJ spin-valve using the single SyAF [Co/Pt]_n layer, at a t_W of 0.16 nm, its *M-H* loop was completely different from that of the spin-valve using the double SyAF [Co/Pt]_n layer; i.e., there was no the squareness in the *M-H* loop for the single SyAF layer (see the red boxes in Fig. 2(a) and (d)). The spin-electron direction of the Co₂Fe₆B₂ pinned layer gradually rotated from upward to downward and saturated as the external perpendicular magnetic-field (*H*) was scanned from +6.5 to +1.5 kOe, (Fig. 2(d)). Then, the spin-electron direction of the Co₂Fe₆B₂ free layer rotated from upward to downward when *H* was scanned from +0.2 to -0.2 kOe, meaning that the free layer showed good perpendicular magnetic characteristics and the TMR ratio was 173%. Finally, the spin-electron direction of the single SyAF [Co/Pt]₃ layer rotated from upward to downward when *H* was scanned from -0.2 to -6.5 kOe, resulting in an H_{ex} of 2.52 kOe, which would be sufficient to avoid a read disturbance failure (Fig. 2(d)). In addition, when t_W was changed from 0.16 to 0.30 nm, the squareness of the *M-H* loop of the Co₂Fe₆B₂ free layer slightly improved, resulting in an increase in the TMR ratio from 173 to 180% (compare the insets of Fig. 2(d), Fig. 2(e), and Fig. 1(c)). H_{ex} of the p-MTJ spin-valve considerably increased from 2.52 to 3.44 kOe, probably improving the read disturbance of p-MTJ spin-valves. Furthermore, when t_W changed from 0.30 to 0.48 nm, the *M-H* loop abnormally deteriorated because the thicker t_W could not perfectly anti-ferro-couple the single SyAF [Co/Pt]₃ layer with the Co₂Fe₆B₂ pinned layer (Fig. 2(f)). In particular, the squareness of the *M-H* loop of the Co₂Fe₆B₂ free layer greatly deteriorated, resulting the TMR ratio falling from 180 to ~0% (see the insets of Fig. 2(e) and (f)). In addition, H_{ex} abruptly dropped from 2.64 to 1.16 kOe, which would probably cause a read disturbance failure. In summary, the *M-H* loop of the p-MTJ spin-valves using a single SyAF [Co/Pt]_n layer had an H_{ex} that was little higher than that of those using a double SyAF [Co/Pt]_n layer, although the total thickness of the SyAF [Co/Pt]_n layer was reduced considerably from 8.65 to 3.55 nm, which would not cause a read disturbance failure. However, the comparison of the *M-H* loops did not explain why the spin-valve using a single SyAF [Co/Pt]_n layer had a higher TMR ratio than those using the double SyAF [Co/Pt]_n layer. Thus, we investigated the face-centered-cubic (f.c.c) crystallinity of the p-MTJ spin-valves by using x-HRTEM. Here we should recall that the f.c.c crystallinity of the MgO tunneling barrier directly affects the probability of coherent tunneling of the spin electrons, determining dominantly the TMR ratio of a p-MTJ spin-valve^{14,17–30}.

Crystallinity of the MgO tunneling barrier. The f.c.c crystallinity of the MgO tunneling barrier was examined in the spin valves with the double SyAF [Co/Pt]_n layer at $t_W = 0.30$ nm (i.e., Fig. 2(b)) and a single SyAF [Co/Pt]_n layer at $t_W = 0.24$ nm (i.e., Fig. 2(e)), as shown in the x-HRTEM images of Fig. 3. The MgO tunneling barrier and capping layer of the spin-valve using the double SyAF [Co/Pt]_n layer had a fluctuating surface like a sinusoidal wave (Fig. 3(a) and (c)). On the other hand, the MgO tunneling barrier and capping layer of the spin-valve using the single SyAF [Co/Pt]_n layer had a flat surface (Fig. 3(b) and (d)). The surface roughness of the tunneling barrier and capping layer became smoother as the SyAF [Co/Pt]_n layer thickness was decreased from 8.65 nm (i.e., a double SyAF [Co/Pt]_n layer) to 3.55 nm (i.e., a single SyAF [Co/Pt]_n layer). In particular, the peak-to-valley of the MgO tunneling barrier (Δ_{p-v}) for the single SyAF [Co/Pt]_n layer (i.e., 1.4 nm for $t_{\text{SyAF}} = 3.55$ nm) was much less than that for the double SyAF [Co/Pt]_n layer (i.e., 2.6 nm for $t_{\text{SyAF}} = 8.65$ nm), as shown in Fig. 3(a) and (b).

Since the f.c.c crystallinity of the MgO tunneling barrier directly influences the coherent tunneling of spin-electrons in the spin-valves, x-HRTEM images of regions **i** and **ii** in Fig. 3(a) and (b) were taken (Fig. 3(c) and (d)). For the spin-valve with a double SyAF [Co/Pt]_n layer, the fluctuating surface of the MgO tunneling barrier and capping layer (Fig. 3(c)) originated from the thicker SyAF [Co/Pt]_n layer ($t_{\text{SyAF}} = 8.65$ nm). In particular, the MgO capping layer showed almost amorphous regions (**a** and **b** in Fig. 3(c)) together with a region of locally f.c.c textured crystallinity (**c** in Fig. 3(c)) and it had a large thickness variation (i.e., ~0.64 nm at **i** and ~0.80 nm at **ii** in Fig. 3(c)). In contrast, the tunneling barrier looked almost completely f.c.c textured (**d** and **e** in Fig. 3(c)) and its thickness was ~0.96 nm at **iii** and 0.86 nm at **iv** in Fig. 3(c). Otherwise, the spin-valve with the single SyAF [Co/Pt]_n layer had a much smoother MgO capping layer than that using the double SyAF [Co/Pt]_n layer, (Fig. 3(c) and (d)) resulting in a uniform capping layer thickness (i.e., ~0.91 nm at **i** and ~0.85 nm at **ii** in Fig. 3(d)). In particular, except at the grain boundaries, the MgO capping layer was almost completely f.c.c, as shown in **a** and **b** in Fig. 3(d). Furthermore, the spin-valve with the single SyAF [Co/Pt]_n layer had a tunneling layer with a flatter surface than that of the one with the double SyAF [Co/Pt]_n layer (Fig. 3(c) and (d)). It had a uniform MgO tunneling barrier layer thickness (i.e., ~1.10 nm at **iii** and ~1.14 nm at **iv** in Fig. 3(d)). This result originated from the thickness difference between the single ($t_{\text{SyAF}} = 1.40$ nm) and double SyAF [Co/Pt]_n layer ($t_{\text{SyAF}} = 8.65$ nm). The MgO tunneling barrier was f.c.c. except at the grain boundaries, as shown in **c** and **d** in Fig. 3(d). In particular, the tunneling barrier (i.e., 1.10~1.14 nm) for the spin-valve using the single SyAF [Co/Pt]_n layer was quite thicker than that of the spin-valve with the double SyAF layer (i.e., 0.86~0.96 nm). These results indicate that the f.c.c. crystallinity of the MgO tunneling-barrier layer for the spin-valve using single SyAF [Co/Pt]_n layer was

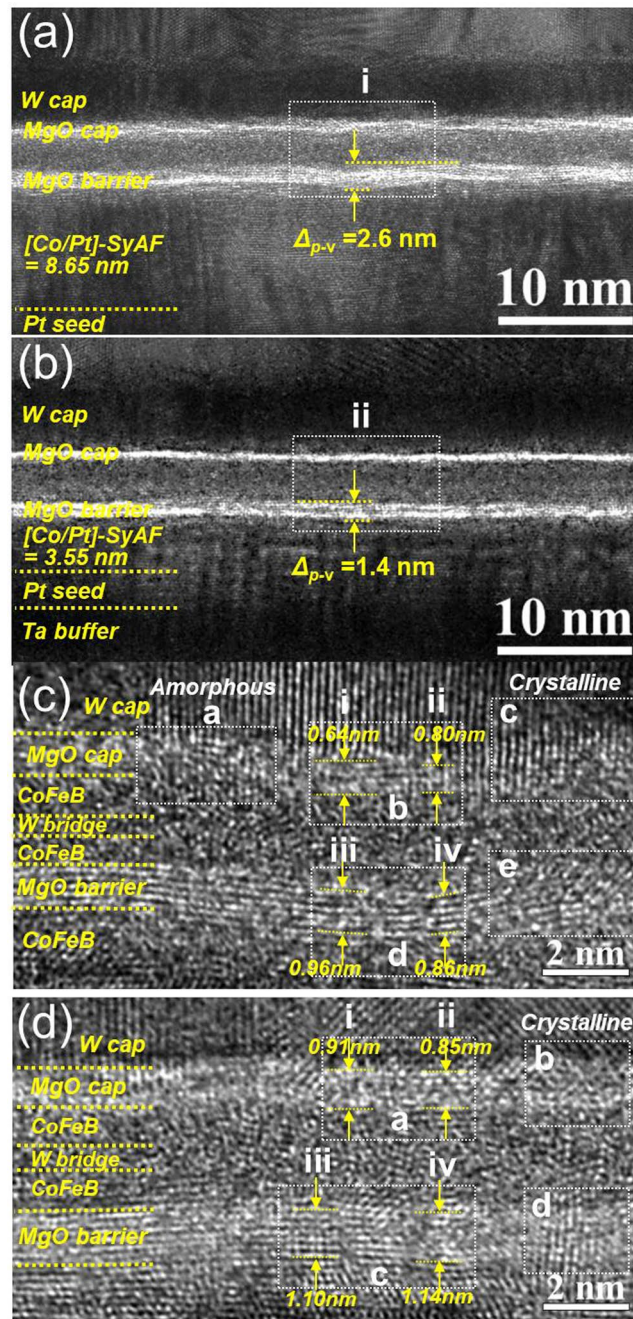


Figure 3. Crystallinity of MgO capping and tunneling layer depending on the p-MTJ spin-valve structure. Low magnification x-HRTEM images of p-MTJ spin-valve using (a) a double SyAF $[\text{Co/Pt}]_n$ layer and (b) a single SyAF $[\text{Co/Pt}]_n$ layer, (c) x-HRTEM images obtained from inset (i) in Fig. 3(a) and (d) x-HRTEM images obtained from inset (ii) in Fig. 3(b).

much superior to that of the spin-valve using the double SyAF $[\text{Co/Pt}]_n$ layer. Here, we should recall that larger surface roughness in the MgO tunneling barrier reduces the hybridization of the Co-O and Fe-O atoms at the interface between the $\text{Co}_2\text{Fe}_6\text{B}_2$ free layer and tunneling barrier which degrades the i-PMA characteristics of the p-MTJ^{20,31,32}. In addition, better f.c.c crystallinity of the MgO tunneling barrier leads to a higher coherent tunneling ability of spin-electrons. Thus, both surface roughness and f.c.c crystallinity directly and dominantly affect the TMR ratio of the p-MTJ spin-valves; i.e., smaller surface roughness and better f.c.c crystallinity of the MgO tunneling barrier leads to a higher TMR ratio^{14,17–30}. Thus, as revealed in the x-HRTEM image, the MgO tunneling barrier of the spin-valve using the single SyAF $[\text{Co/Pt}]_n$ layer obviously showed a smaller surface roughness and better f.c.c crystallinity compared with the barrier of the spin-valve with the double SyAF $[\text{Co/Pt}]_n$ layer. As a result, the p-MTJ spin-valve using the single SyAF $[\text{Co/Pt}]_n$ layer (~180%) achieved a higher TMR ratio than that of the one using the double SyAF $[\text{Co/Pt}]_n$ layer (~156%).

Discussion

Double MgO-based p-MTJ spin-valve with a top $\text{Co}_2\text{Fe}_6\text{B}_2$ free layer using a double SyAF $[\text{Co}/\text{Pt}]_n$ layer (Fig. 1(a)) have been intensively studied in order to achieve TMR ratios higher than 150% in order to ensure a memory margin and enough thermal stability (Δ) for a ten-year retention-time at BEOL temperatures higher than 350 °C. However, the high surface roughness of the MgO tunneling barrier that originates from the thick double SyAF $[\text{Co}/\text{Pt}]_n$ layer (i.e., 8.65 nm) potentially limits further enhancement of the TMR ratio. As a solution, a double MgO-based p-MTJ spin-valve structure with a top $\text{Co}_2\text{Fe}_6\text{B}_2$ free layer using a single SyAF $[\text{Co}/\text{Pt}]_n$ layer (Fig. 1(b)) was developed that has a thinner single SyAF $[\text{Co}/\text{Pt}]_n$ layer (i.e., 3.55 nm) and a buffer layer bridging the single SyAF $[\text{Co}/\text{Pt}]_n$ layer and the $\text{Co}_2\text{Fe}_6\text{B}_2$ pinned layer (i.e., Co/Pt/Co layer). This device structure demonstrated a sufficient anisotropy exchange field (i.e. 3.44 kOe) for avoiding read disturbance failures and a TMR ratio about 25% higher than that of a p-MTJ spin-valve using double SyAF $[\text{Co}/\text{Pt}]_n$ layer. In particular, the f.c.c crystallinity of the MgO tunneling barrier was improved by the greatly reduced surface roughness of the MgO tunneling barrier (i.e., 1.4 nm). Therefore, the double MgO-based p-MTJ spin-valve with a top $\text{Co}_2\text{Fe}_6\text{B}_2$ free layer using a single SyAF layer would be a promising spin-valve structure for future device application such as a terra-bit integration stand-alone memory, an embedded memory, a storage class memory, etc.

Methods

All double MgO-based p-MTJ spin-valves were fabricated using a 12-inch-wafer multi-chamber cluster-magnetron sputtering-system under a high vacuum of less than 1×10^{-8} torr. In particularly, the double MgO-based p-MTJ spin-valve structure with a top $\text{Co}_2\text{Fe}_6\text{B}_2$ free layer using a double SyAF $[\text{Co}/\text{Pt}]_n$ layer were fabricated as a vertical stack containing a 12-inch SiO_2 wafer, W/TiN bottom electrode, Ta buffer layer, Pt seed layer, $[\text{Co}(0.4 \text{ nm})/\text{Pt}(0.3 \text{ nm})]_6/\text{Co}(0.6 \text{ nm})$ lower SyAF layer, Ru spacer layer (0.85 nm), $\text{Co}(0.6 \text{ nm})/\text{Pt}(0.3 \text{ nm})/[\text{Co}(0.4 \text{ nm})/\text{Pt}(0.3 \text{ nm})]_3$ upper SyAF layers, and a Co buffer layer (0.4 nm), as shown in Fig. 1(a). The thickness of the tungsten (W) bridge layer was varied from 0.18 nm to 0.48 nm, and the p-MTJ consisted of a $\text{Co}_2\text{Fe}_6\text{B}_2$ pinned layer (1.05 nm), MgO tunneling barrier (1.2 nm), Fe insertion layer (0.44 nm), $\text{Co}_2\text{Fe}_6\text{B}_2$ free layer (1.0 nm), W spacer layer (0.4 nm), $\text{Co}_2\text{Fe}_6\text{B}_2$ (1.0 nm), and MgO (1.0 nm)/W capping layer. The double MgO-based p-MTJ spin-valve with a top $\text{Co}_2\text{Fe}_6\text{B}_2$ free layer using a single SyAF $[\text{Co}/\text{Pt}]_n$ layer were fabricated wherein the ratio of the number of $[\text{Co}/\text{Pt}]$ multi-layers between the upper and lower SyAF $[\text{Co}/\text{Pt}]_n$ layer was varied from 3:6 (i.e., a double SyAF $[\text{Co}/\text{Pt}]_n$ layer) to 0:3, as shown in Fig. 2 (b). In addition, the bridging buffer layer was a Co/Pt/Co layer instead of the single Co layer (compare Fig. 1(a) and (b)). Note that the bridging buffer layer is necessary to ferro-couple the $\text{Co}_2\text{Fe}_6\text{B}_2$ free layer with the SyAF $[\text{Co}/\text{Pt}]_n$ layer. The spin-valves were *ex-situ* annealed at 350 °C for 30 min under a vacuum below 10^{-6} torr and a perpendicular magnetic field of 3 tesla. The TMR ratios of the 12-inch wafer p-MTJ spin-valves were estimated by using current in-plane tunneling (CIPT) at room temperature. Afterward, the wafers were cut into $1 \times 1 \text{ cm}^2$ pieces. The magnetic properties (out-of-plane and in-plane) for the two different spin-valves were characterized by using vibrating sampling magnetometer (VSM) at room temperature. The crystallinity was estimated by using x-HRTEM at an acceleration voltage of 200 keV.

References

- Kang, S. H. Embedded STT-MRAM for energy-efficient and cost-effective mobile systems. *Digest of Technical Papers - Symposium on VLSI Technology* **4446**, 2013–2014 (2013).
- Halawani, Y., Mohammad, B., Homouz, D., Al-Qutayri, M. & Saleh, H. Modeling and optimization of memristor and STT-RAM-based memory for low-power applications. *IEEE Transactions on Very Large Scale Integration (VLSI) Systems* **24**(3), 1003–1014 (2016).
- Grollier, J., Querlioz, D. & Stiles, M. D. Spintronic Nanodevices for Bioinspired Computing. *Proc IEEE Inst Electr Electron Eng.* **104**(10), 2024–2039 (2016).
- Vincent, A. F. *et al.* Spin-transfer torque magnetic memory as a stochastic memristive synapse for neuromorphic systems. *IEEE Transactions on Biomedical Circuits and Systems* **9**(2), 166–174 (2015).
- Park, J. G. *et al.* Challenging issues for terra-bit-level perpendicular STT-MRAM. *IEEE Int. Electron Devices Meeting, IEDM 2015–February*, 19.2.1–19.2.4 (2015).
- Kent, A. D. & Worledge, D. C. A new spin on magnetic memories. *Nature Nanotechnology* **10**(3), 187–191 (2015).
- Lu, Y. *et al.* Fully functional perpendicular STT-MRAM macro embedded in 40 nm logic for energy-efficient IOT applications. *IEEE Int. Electron Devices Meeting, IEDM 2016–February*, 26.1.1–26.1.4 (2016).
- Aitken, R. *et al.* Device and technology implications of the Internet of Things. *2014 Symp. VLSI Technol. Dig. Tech. Papers*, 1–4 (2014).
- Ohno, H., Endoh, T., Hanyu, T., Kasai, N. & Ikeda, S. Magnetic tunnel junction for nonvolatile CMOS logic. *IEEE Int. Electron Devices Meeting*, 9.A.1–9.A.4 (2010).
- Ikeda, S. *et al.* A perpendicular-anisotropy CoFeB–MgO magnetic tunnel junction. *Nature Materials* **9**(9), 721–724 (2010).
- Slonczewski, J. C. Ferromagnetic tunnel junction, magnetoresistive element and magnetic head. US patent 5, 862,022, Jan. 19, (1999).
- Wen, Z. *et al.* A 4-Fold-Symmetry Hexagonal Ruthenium for Magnetic Heterostructures Exhibiting Enhanced Perpendicular Magnetic Anisotropy and Tunnel Magnetoresistance. *Adv. Mater.* **26**(37), 6483–6490 (2014).
- Honjo, H. *et al.* 10 nm φ perpendicular-anisotropy CoFeB–MgO magnetic tunnel junction with over 400 °C high thermal tolerance by boron diffusion control. *2015 Symp. VLSI Technol. Dig. Tech. Papers*, 160–161 (2015).
- Lee, D. Y., Lee, S. E., Shim, T. H. & Park, J. G. Tunneling-Magnetoresistance Ratio Comparison of MgO-Based Perpendicular-Magnetic-Tunneling-Junction Spin Valve Between Top and Bottom $\text{Co}_2\text{Fe}_6\text{B}_2$ Free Layer Structure. *Nanoscale Research Letters* **11**(1), 433 (2016).
- Sato, H. *et al.* Perpendicular-anisotropy CoFeB–MgO magnetic tunnel junctions with a MgO/CoFeB/Ta/CoFeB/MgO recording structure. *App. Phys. Lett.* **101**(2), 022414 (2012).
- Sato, H. *et al.* MgO/CoFeB/Ta/CoFeB/MgO recording structure in magnetic tunnel junctions with perpendicular easy axis. *IEEE Transactions on Magnetics* **49**(7), 4437–4440 (2013).
- Lee, S. E., Takemura, Y. & Park, J. G. Effect of double MgO tunneling barrier on thermal stability and TMR ratio for perpendicular MTJ spin-valve with tungsten layers. *App. Phys. Lett.* **109**(18), 182405 (2016).

18. Lee, D. Y., Hong, S. H., Lee, S. E. & Park, J. G. Dependency of Tunneling-Magnetoresistance Ratio on Nanoscale Spacer Thickness and Material for Double MgO Based Junction. *Scientific Reports* **6**, 38125 (2016).
19. Lee, S. E., Shim, T. H. & Park, J. G. Perpendicular magnetic tunnel junction (p-MTJ) spin-valves designed with a top Co₂Fe₆B₂ free layer and a nanoscale-thick tungsten bridging and capping layer. *NPG Asia Materials* **8**(11), e324 (2016).
20. Shen, W. *et al.* Effect of film roughness in MgO-based magnetic tunnel junctions. *App. Phys. Lett.* **88**(18), 182508 (2006).
21. Ikeda, S. *et al.* Dependence of tunnel magnetoresistance in MgO based magnetic tunnel junctions on Ar pressure during MgO sputtering. *Jpn. J. Appl. Phys.* **44**(48), L1442–L1445 (2005).
22. Jeon, M. S. *et al.* The dependency of tunnel magnetoresistance ratio on nanoscale thicknesses of Co₂Fe₆B₂ free and pinned layers for Co₂Fe₆B₂/MgO-based perpendicular-magnetic-tunnel-junctions. *Nanoscale* **7**(17), 8142–8148 (2015).
23. Chae, K. S. & Park, J. G. Dependency of tunneling magneto-resistance on Fe insertion-layer thickness in Co₂Fe₆B₂/MgO-based magnetic tunneling junctions. *J. Appl. Phys.* **117**, 153901 (2015).
24. Lee, D. Y., Seo, H. T. & Park, J. G. Effects of the radio-frequency sputtering power of an MgO tunneling barrier on the tunneling. *J. Mater. Chem. C* **4**, 135–141 (2016).
25. Lee, D. Y., Shim, T. H. & Park, J. G. Effect of coupling ability between a synthetic antiferromagnetic layer and pinned layer on a bridging layer of Ta, Ti, and Pt in perpendicular-magnetic tunnel junctions. *Nanotechnology* **27**(29), 295705 (2016).
26. Lee, D. Y., Shim, T. H. & Park, J. G. Effects of Pt capping layer on perpendicular magnet anisotropy in pseudo-spin valves of Ta/CoFeB/MgO/CoFeB/Pt magnetic-tunneling junctions. *App. Phys. Lett.* **102**(21), 212409 (2013).
27. Takemura, Y. *et al.* Influence of face-centered-cubic texturing of Co₂Fe₆B₂ pinned layer on tunneling magnetoresistance ratio decrease in Co₂Fe₆B₂/MgO-based p-MTJ spin valves stacked with a [Co/Pd]_n-SyAF layer. *Nanotechnology* **26**(19), 195702 (2015).
28. Lee, S. E., Shim, T. H. & Park, J. G. Co₂Fe₆B₂/MgO-based perpendicular spin-transfer-torque magnetic-tunnel-junction spin-valve without [Co/Pt]_n lower synthetic-antiferromagnetic layer. *Nanotechnology* **26**(47), 475705 (2015).
29. Takemura, Y., Lee, D. Y., Lee, S. E. & Park, J. G. Dependency of tunneling magnetoresistance ratio on Pt seed-layer thickness for double MgO perpendicular magnetic tunneling junction spin-valves with a top Co₂Fe₆B₂ free layer *ex-situ* annealed at 400°C. *Nanotechnology* **27**(48), 485203 (2016).
30. Chae, K. S., Shim, T. H. & Park, J. G. Dependency of anti-ferro-magnetic coupling strength on Ru spacer thickness of [Co/Pd]_n-synthetic-anti-ferro-magnetic layer in perpendicular magnetic-tunnel-junctions fabricated on 12-inch TiN electrode wafer. *J. Appl. Phys.* **116**(3), 033904 (2014).
31. Yang, H. X. *et al.* First-principles investigation of very large perpendicular magnetic anisotropy at Fe|MgO and Co|MgO interfaces. *Phys. Rev. B* **84**, 054401 (2011).
32. Chae, K. S., Lee, D. Y., Shim, T. H., Hong, J. P. & Park, J. G. Correlation of the structural properties of a Pt seed layer with the perpendicular magnetic anisotropy features of full Heusler-based Co₂FeAl/MgO/Co₂Fe₆B₂ junctions via a 12-inch scale Si wafer process. *App. Phys. Lett.* **103**, 162409 (2013).

Acknowledgements

This work was supported by Basic Science Research Program through the National Research Foundation of Korea (NRF) grant funded by the Korea government (MSIP) (No. 2017R1A2A1A05001285) and Brain Korea 21 PLUS Program in 2014.

Author Contributions

J.Y. Choi and J.G. Park conceived and designed the study. J.Y. Choi and J.U. Baek fabricated all patterns and carried out experiments, with the help of J.G. Park. Contributions to the measurements were made by J.Y. Choi, D.G. Lee and J.U. Baek. All authors contributed to discussions regarding the research. J.Y. Choi and J.G. Park wrote the manuscript.

Additional Information

Supplementary information accompanies this paper at <https://doi.org/10.1038/s41598-018-20626-4>.

Competing Interests: The authors declare no competing interests.

Publisher's note: Springer Nature remains neutral with regard to jurisdictional claims in published maps and institutional affiliations.



Open Access This article is licensed under a Creative Commons Attribution 4.0 International License, which permits use, sharing, adaptation, distribution and reproduction in any medium or format, as long as you give appropriate credit to the original author(s) and the source, provide a link to the Creative Commons license, and indicate if changes were made. The images or other third party material in this article are included in the article's Creative Commons license, unless indicated otherwise in a credit line to the material. If material is not included in the article's Creative Commons license and your intended use is not permitted by statutory regulation or exceeds the permitted use, you will need to obtain permission directly from the copyright holder. To view a copy of this license, visit <http://creativecommons.org/licenses/by/4.0/>.

© The Author(s) 2018